Monthly Notices
of the
ROYAL ASTRONOMICAL SOCIETY

MNRAS **467,** 2571–2584 (2017)
Advance Access publication 2017 January 27

doi:10.1093/mnras/stx231

Quasar emission lines as probes of orientation: implications for disc wind geometries and unification

J. H. Matthews,[1,2]★ C. Knigge[2] and K. S. Long[3,4]

[1]*Astrophysics, Department of Physics, University of Oxford, Keble Road, Oxford OX1 3RH, UK*
[2]*School of Physics and Astronomy, University of Southampton, Highfield, Southampton SO17 1BJ, UK*
[3]*Space Telescope Science Institute, 3700 San Martin Drive, Baltimore, MD 21218, USA*
[4]*Eureka Scientific, Inc., 2452 Delmer Street Suite 100, Oakland, CA 94602-3017, USA*

Accepted 2017 January 24. Received 2017 January 16; in original form 2016 November 11

ABSTRACT

The incidence of broad absorption lines (BALs) in quasar samples is often interpreted in the context of a geometric unification model consisting of an accretion disc and an associated outflow. We use the Sloan Digital Sky Survey quasar sample to test this model by examining the equivalent widths (EWs) of C IV 1550 Å, Mg II 2800 Å, [O III] 5007 Å and C III] 1909 Å. We find that the emission line EW distributions in BAL and non-BAL quasars are remarkably similar – a property that is inconsistent with scenarios in which a BAL outflow rises equatorially from a geometrically thin, optically thick accretion disc. We construct simple models to predict the distributions from various geometries; these models confirm the above finding and disfavour equatorial geometries. We show that obscuration, line anisotropy and general relativistic effects on the disc continuum are unlikely to hide an EW inclination dependence. We carefully examine the radio and polarization properties of BAL quasars. Both suggest that they are most likely viewed (on average) from intermediate inclinations, between type 1 and type 2 active galactic nuclei (AGN). We also find that the low-ionization BAL quasars in our sample are not confined to one region of the 'Eigenvector 1' parameter space. Overall, our work leads to one of the following conclusions, or some combination thereof: (i) the continuum does not emit like a geometrically thin, optically thick disc; (ii) BAL quasars are viewed from similar angles to non-BAL quasars, that is, low inclinations and (iii) geometric unification does not explain the fraction of BALs in quasar samples.

Key words: accretion, accretion discs – galaxies: active – quasars: emission lines – quasars: general.

1 INTRODUCTION

The ultraviolet (UV) and optical spectra of type 1 quasars are characterized by a blue continuum and a series of broad and narrow emission lines. Approximately 20 per cent of quasars also show blueshifted, broad absorption lines (BALs) in their UV spectra (Weymann et al. 1991; Knigge et al. 2008; Allen et al. 2011), providing clear evidence that outflowing material intersects the line of sight to the continuum source. Most BAL quasars (BALQs) exhibit only high-ionization BALs (HiBALs), but a subset (∼10 per cent) also shows absorption in lower ionization species such as Mg II and is known as low-ionization BAL quasars (LOBALQs; e.g. Reichard et al. 2003).

The BAL phenomenon is normally explained either by evolutionary models (Becker et al. 2000; Gregg et al. 2000; Gregg, Becker & de Vries 2006; Farrah et al. 2007; Lipari et al. 2009), in which quasars spend ∼20 per cent of their lifetime as BALQs, or by a geometric interpretation, in which the BAL fraction roughly corresponds to the covering factor of an ever-present wind (Murray et al. 1995; Elvis 2000). In the latter case, winds could also create the broad emission lines seen in quasar spectra, meaning that they offer a natural avenue through which the diverse phenomenology of quasars can be *unified* according to orientation. This principle of geometric unification is not confined to disc wind models; orientation-based models have also been famously invoked to explain the type 1/type 2 and radio-loud/radio-quiet dichotomies in active galactic nuclei (AGNs; Antonucci & Miller 1985; Urry & Padovani 1995), as well as the 'Eigenvector 1' (EV1) trend in quasars (Boroson & Green 1992; Marziani et al. 2001; Shen & Ho 2014).

Geometric unification scenarios require – by definition – that different classes of objects are viewed from different angles. They thus predict that any orientation-dependent observable should vary accordingly between the classes. Empirical (albeit model-dependent)

★ E-mail: james.matthews@physics.ox.ac.uk

examples include the differences in polarization properties (e.g. Marin 2014) and absorbing column densities (e.g. Lusso et al. 2012) between type 1 and type 2 AGNs. However, in general, obtaining reliable orientation indicators in quasars and AGNs is difficult (see Marin 2016, for a summary). Perhaps as a result of this problem, directly opposing geometries have been proposed for BAL outflows themselves. Polarization studies imply that the wind is roughly equatorial (Cohen et al. 1995; Goodrich & Miller 1995; Lamy & Hutsemékers 2004; Brotherton, De Breuck & Schaefer 2006), as also suggested by hydrodynamical and radiative transfer simulations (Proga, Stone & Kallman 2000; Proga & Kallman 2004; Borguet & Hutsemékers 2010; Higginbottom et al. 2013). However, there is also evidence for polar BAL outflows in radio-loud (RL) sources (Zhou et al. 2006; Ghosh & Punsly 2007).

One potential orientation indicator is the equivalent width (EW) of the emission lines (e.g. Risaliti, Salvati & Marconi 2011). The UV-optical continuum in AGNs, known as the big blue bump, is normally thought to originate from a geometrically thin, optically thick accretion disc surrounding the central black hole (e.g. Shields 1978; Malkan & Sargent 1982; Malkan 1983; Capellupo et al. 2015). The emission from this disc should be strongly anisotropic due to foreshortening and possibly limb darkening (e.g. Herter et al. 1979; Wade 1984; Laor & Netzer 1989; Hubeny et al. 2000, see also Section 3.1). On the other hand, there is no a priori reason why emission lines should emit in the same manner as the disc. If a line is at all optically thin, or formed in a region with isotropic escape probabilities, then the emission will radiate isotropically (see Section 3.3). It follows that we might expect emission line EW to increase with inclination and be largest for edge-on systems, especially for optically thin narrow emission lines.

The variation of EW with inclination is demonstrated neatly by the behaviour of emission lines in high-state accreting white dwarfs (AWDs), often thought to be reasonable quasar analogues. In these systems, inclinations are more well constrained and a geometrically thin, optically thick accretion disc is established as the continuum source (Warner 1995, and references therein). High-state AWDs do indeed show a clear trend of increasing line EW with inclination (Hessman et al. 1984; Patterson 1984; Echevarria 1988). This behaviour is also seen in radiative transfer simulations in both AWDs and quasars (Noebauer et al. 2010; Matthews et al. 2015, 2016). The upshot is that quasar line EWs could potentially be used (i) to test geometric unification models for, e.g. quasars and the BAL phenomenon, or (ii) to help understand the origin of the UV-optical continuum in AGNs. The latter is particularly important given the currently unsatisfactory understanding of the quasar continuum source (e.g. Koratkar & Blaes 1999, see also Section 3).

The ideal emission line to use for this method would be one that is completely isotropic, that is, *optically thin*. The [O III] 5007 Å narrow emission line fulfils this criterion, since it is a strong, forbidden line formed in the narrow-line region (NLR) of an AGN. Any dispersion in the distribution of [O III] 5007 Å EW (EW[O III]) must therefore be driven by some combination of the intrinsic luminosity (Boroson & Green 1992), the covering factor/geometry of the NLR (Baskin & Laor 2005) and the inclination of the disc (Risaliti et al. 2011). In a recent study, Risaliti et al. (2011, hereafter R11) showed that the EW[O III] distribution had a high power-law tail and could be well fitted by a simple model driven purely by disc inclination. In this study, we compare the EWs of a number of emission lines in BAL and non-BALQ samples in order to test unification models in which the continuum source is a geometrically thin, optically thick accretion disc. Our study is motivated by the remarkably similar emission line properties of BAL and non-BALQs (see Fig. 1) – a similarity that would not be expected from simple models in which BALQs are viewed from equatorial angles.

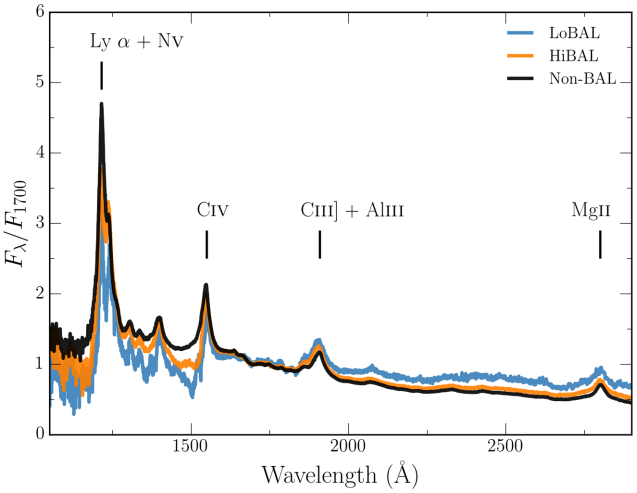

Figure 1. SDSS composite spectra for HiBAL, LoBAL and non-BALQs from Reichard et al. (2003). The prominent emission lines are marked and the spectra are normalized to the monochromatic flux at 1700 Å.

This paper is structured as follows. First, we describe the data sample and selection criteria being used. We begin by simply examining the BAL and non-BALQ distributions for four emission lines: the narrow [O III] 5007 Å line and the broad C IV 1550 Å, C III] 1909 Å and Mg II 2800 Å lines. We construct some simple toy geometric models in which an optically thick, geometrically thin disc acts as the continuum source and BALQs are viewed from some subset of angles dependent on the geometry of the BAL outflow. We find, as expected, that such toy models predict large differences in EW distributions if BALs are only seen at high inclinations. Our discussion begins in Section 3, in which we first explore if there are any straightforward explanations – namely general relativistic effects, line anisotropy or obscuration – that could readily explain the EW distribution and allow BALQs to be seen at systematically different inclinations to non-BALQs. In Section 4, we discuss the results in the context of radio and polarization measurements of AGNs, and explore the location of BALQs in the 'EV1' parameter space. Finally, in Section 5, we summarize our results.

2 THE EW DISTRIBUTIONS OF BAL AND NON-BALQS

Our data samples are based on two catalogues from the Sloan Digital Sky Survey (SDSS): the Shen et al. (2011, hereafter S11) catalogue of 105 783 quasars from the SDSS Data Release (DR) 7 (Abazajian et al. 2009) and the Pâris et al. (2017, hereafter P16) catalogue of 297 301 quasars from the SDSS DR 12. As we will use emission line diagnostics in this study, our samples must be divided according to which emission lines are present in the SDSS wavelength range at a given redshift. Sample A contains all quasars from S11[1] within the redshift range $0.35 < z < 0.83$, such that the Mg II 2800 Å and [O III] 5007 Å line EWs are both measured and Mg II LoBAL

[1] Note that although Albareti et al. (2015) present a more recent compendium of [O III] 5007 Å line measurements based on DR12, the catalogue actually contains less quasars in total than S11, so we revert to DR7 for sample A. This is due to the coverage of the samples at $z < 0.83$ (P16).

Table 1. A summary of the data samples described in the text. HiBAL identification is not possible in sample A due to the wavelength coverage.

Sample	Size	$N_{\rm BAL}$	Redshift range	Lines used	Source
A	16 742	58 (all LoBAL)	$0.35 < z < 0.83$	Mg II 2800 Å, [O III] 5007 Å	S11/DR7
B	80 429	6744	$1.45 < z < 2.28$	Mg II 2800 Å, C III] 1909 Å, C IV 1550 Å	P16/DR12

identification is possible. Sample B contains all quasars from P16 within the redshift range $1.45 < z < 2.28$, such that the EWs and presence of BALs in Mg II 2800 Å, C III] 1909 Å and C IV 1550 Å are both measurable. The samples are summarized in Table 1.

S11 are careful to take into account traditional problems with quasar line fitting, such as narrow-line or Fe pseudo-continuum contamination, in their fits to emission line profiles and resultant EW measurements. For Mg II 2800 Å, this includes careful subtraction of the nearby Fe emission using the Vestergaard & Wilkes (2001) templates. This subtraction is not included for C IV 1550 Å, as the Fe emission is less prominent and harder to model. This may lead to a systematic overestimate by ∼0.05 dex in the C IV line EW. The [O III] 5007 Å line is fitted with a Gaussian. The flux ratio of this line with the sister component of the doublet, [O III] 4959 Å, is found to agree well with the theoretical expectation of around 3, implying a reliable subtraction of broad Hβ. In order to mask out the effects of, e.g. absorption, on the C IV and Mg II lines, S11 ignore 3σ outliers in the fit to the profile. Although P16 provide less detail on the emission line fitting process, we have verified that the EWs of emission lines measured in both P16 and S11 have very similar means and variances, although some differences in shape occur, possibly due to the changes in quasar target selection (see P16). Adopting a different SDSS quasar catalogue does therefore not affect any of our conclusions. The quasar selection criteria for the SDSS DR7 and DR12 are described by Schneider et al. (2010) and Ross et al. (2012), respectively. In S11, the quasars must have at least one broad line, whilst in our P16 sample we only consider broad emission lines; the non-BALQs discussed in the next section are thus unobscured, type 1 quasars with broad emission lines. This means we do not consider obscured, type 2 quasars in our analysis, although we note that the geometry of the model discussed in Section 2.2 could contribute to type 2 observational biases (Reyes et al. 2008; Alexandroff et al. 2013; Yuan, Strauss & Zakamska 2016).

Based on all the above considerations, the S11 and P16 catalogues make for a reliable set of EW measurements. This is especially true when making inferences from multiple emission lines, as systematics inherent to individual lines or spectral windows are less likely to affect the analysis as a whole. Importantly, the data samples chosen allow for emission lines formed in different regions [the broad-line region (BLR) and NLR] and by different atomic transitions (forbidden, intercombination and permitted dipole) to be studied.

2.1 The observed EW distributions

It is apparent from the composite spectra of BAL and non-BALQs (Fig. 1) that, when one compensates for how the blueshifted absorption affects the composites, BAL and non-BALQs seem to possess very similar emission line properties. This has been noted by, e.g. Weymann et al. (1991) in the past. Composite spectra could, however, hide differences between the two populations since they are built from a geometric mean (Reichard et al. 2003). We thus show histograms of EWs for a number of different emission lines in Fig. 2. We give the mean, median and standard deviations of each of these distributions in Table 2, as well as the quantity $\sigma_{\rm m}$, which gives the (asymmetric) distances either side of the median to the 16th and 84th percentiles of the cumulative distribution function. This quantity therefore encloses 68 per cent of the total counts. We also show the difference between the means of the BAL and non-BAL distributions. We mark $\sigma_{\rm m}$, the mean and the median in Fig. 2. In addition, we performed a two-tailed Kolgomorov–Smirnov (KS) test on each of the samples. The p values from these tests are very small in each case. The largest p value obtained is 0.0027 for the smallest sample ([O III]), showing that we can reject the KS null hypothesis at $>3\sigma$ in each case. However, this gives no real information about orientation as the KS null hypothesis will also be rejected when there are small differences in the intrinsic populations and even when the BALQ EWs are systematically *lower* than non-BALQ EWs. This means that the KS test has very limited use in this circumstance.

The EW of an isotropic line is related to the intrinsic, 'face-on' equivalent width, $\rm EW_*$, by the equation

$$\rm EW = EW_*/\epsilon(\theta), \tag{1}$$

where θ is the viewing angle with respect to the symmetry axis and $\epsilon(\theta)$ is the 'angular emissivity function', which describes how the continuum luminosity from the disc varies as a function of viewing angle. For a foreshortened disc, this is simply $\epsilon(\theta) = \cos\theta$. Note that isotropic line emission may not be a reasonable assumption for optically thick permitted dipole transitions and possibly even semiforbidden intercombination lines such as C III] 1909 Å (Bhatia & Kastner 1992); the effect of line anisotropy is discussed further in Section 3.3.

If BALQs are preferentially viewed from larger-than-average angles, we would expect them to possess higher EWs. As shown in Fig. 2 and Table 2, the BALQ mean EW values are not higher than for non-BALQs – in fact, in most cases they are lower. Furthermore, the distribution shapes are generally very similar. Similar EW distributions are not expected from a model in which the continuum comes from a foreshortened disc and BAL outflows are at all equatorial. To examine this apparent discrepancy more concretely, we now devote some time to simulating the expected BAL and non-BAL EW distributions from different unification geometries.

2.2 Expected EW distributions: toy models

A schematic showing the geometry used in our numerical simulations is shown in Fig. 3. In order to test geometric unification scenarios such as that proposed by Elvis (2000), we assume that BALs can be seen in spectra when the viewing angle with respect to the symmetry axis is between θ_1 and θ_2. Non-BALQs are seen when $\theta < \theta_1$. Beyond θ_2, we assume that the object is obscured and does not appear in the quasar sample, as it only consists of type 1 objects. We also define the 'bending angle' of the BAL outflow, which is simply

$$\theta_{\rm b} = (\theta_1 + \theta_2)/2, \tag{2}$$

and the opening angle, which is $\Delta\theta = (\theta_2 - \theta_1)$. These angles are marked in Fig. 3 and are similar to those used by Elvis (2000) and Marin & Goosmann (2013) to describe equivalent geometries.

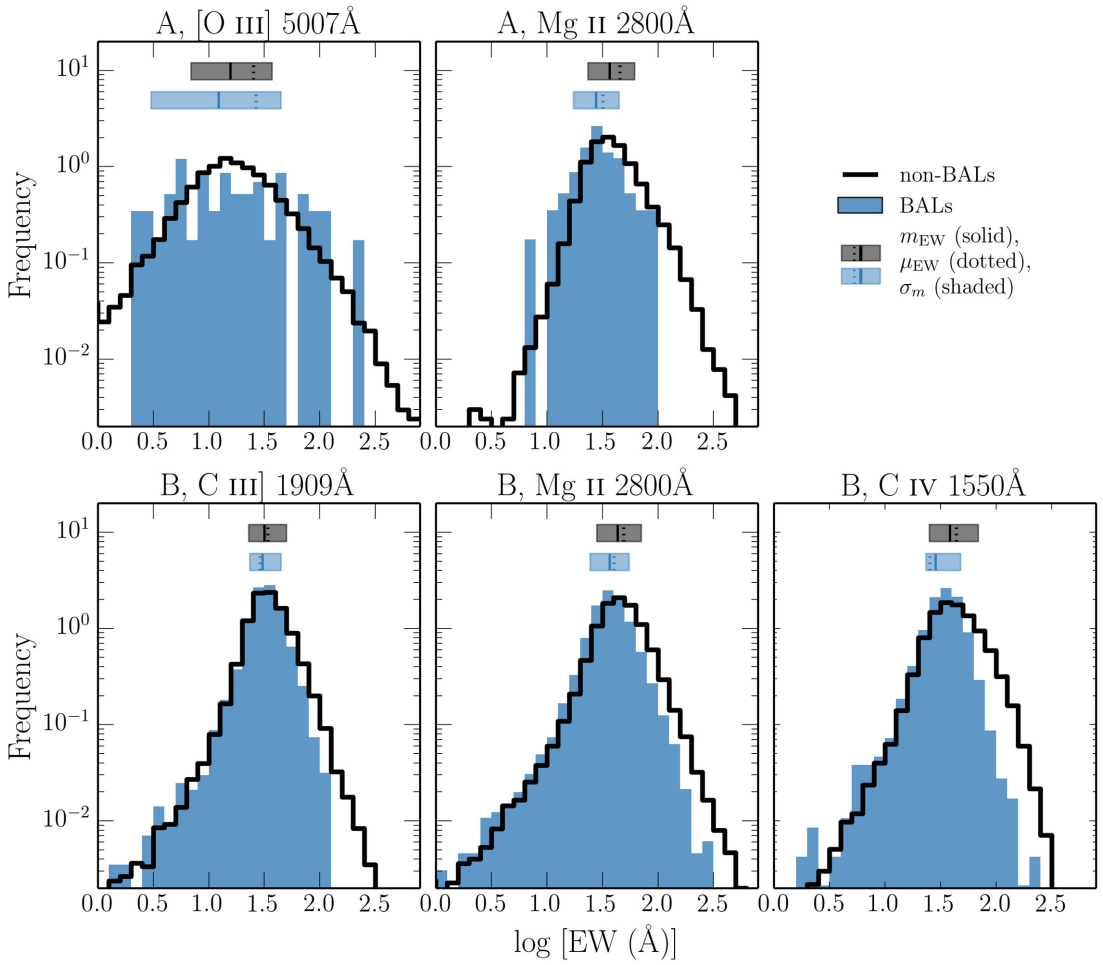

Figure 2. Normalized histograms of EW for different emission lines from the two different samples. The top two panels show the distributions from sample A for the forbidden [O III] 5007 Å line and permitted dipole transition Mg II 2800 Å. The bottom three panels show the distributions from sample B for the semiforbidden/intercombination line C III] 1909 Å and the permitted dipole transitions Mg II 2800 Å and C IV 1550 Å. In all cases, the non-BALQ distributions are plotted with a black line and the BALQs with a solid blue histogram. The binning is logarithmic. The mean ($\mu_{\rm EW}$), median ($m_{\rm EW}$) and $\sigma_{\rm m}$ are defined in the text.

Table 2. The mean ($\mu_{\rm EW}$), median ($m_{\rm EW}$) and standard deviation ($\sigma_{\rm EW}$) of each EW distribution used in this study, for both BAL and non-BALQs. The distributions are shown in Fig. 2. The quantity $\sigma_{\rm m}$ gives the (asymmetric) distances either side of the median to the 16th and 84th percentiles of the cumulative distribution function, thus enclosing 68 per cent of the total counts. Units are in Å. All values are given to two-decimal places.

		non-BAL				BAL				
Sample	line	$\mu_{\rm EW}$	$m_{\rm EW}$	$\sigma_{\rm m}$	$\sigma_{\rm EW}$	$\mu_{\rm EW}$	$m_{\rm EW}$	$\sigma_{\rm m}$	$\sigma_{\rm EW}$	$\Delta\mu_{\rm EW}$
A	[O III] 5007 Å	25.20	15.70	$^{+21.45}_{-8.78}$	36.92	26.76	12.30	$^{+32.37}_{-9.28}$	39.25	1.56 ± 5.16
A	Mg II 2800 Å	45.74	36.80	$^{+24.86}_{-13.36}$	41.42	32.55	27.80	$^{+16.87}_{-10.42}$	16.90	−13.19 ± 2.26
B	C III] 1909 Å	38.13	33.62	$^{+16.50}_{-10.71}$	22.45	34.67	32.57	$^{+12.09}_{-9.13}$	14.67	−3.46 ± 0.21
B	Mg II 2800 Å	52.40	45.01	$^{+25.79}_{-16.82}$	40.35	41.39	37.15	$^{+17.80}_{-12.61}$	21.64	−11.01 ± 0.31
B	C IV 1550 Å	48.51	40.86	$^{+28.32}_{-15.74}$	29.81	36.68	34.74	$^{+13.12}_{-11.30}$	15.09	−11.83 ± 0.25

We carried out the following procedure to simulate the effect of inclination on the EW distributions. This method is similar to that used by R11 to fit the observed EW[O III] distribution in quasars. However, this is not an attempt to fit the data, merely to demonstrate the expected geometric trends.

(i) An isotropic angle was chosen for the mock quasar. If $\theta < \theta_1$, then the mock quasar was designated as a non-BALQ. If $\theta_1 < \theta \leq \theta_2$, the mock quasar was designated as a BALQ and otherwise the object was ignored.

(ii) For each mock sample, an EW_* was drawn from an intrinsic (i.e. 'face-on') EW distribution for quasars, g(EW). To test both symmetric and asymmetric intrinsic distributions, this was assumed to take the form of a normal or lognormal distribution, following R11.[2]

[2] The mean, μ_*, and width, σ_*, of the g(EW) distribution are set by hand to give a reasonable approximation to the observed non-BALQ distribution, but we have also verified that the exact shape does not have a significant effect

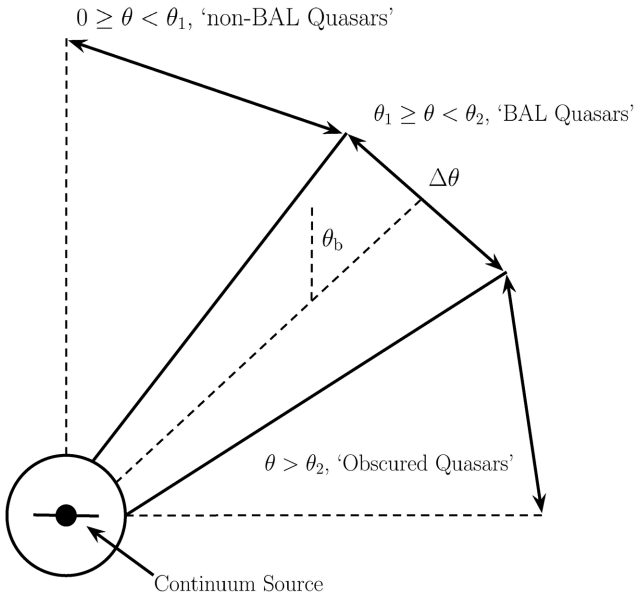

Figure 3. The geometry of the toy model used to carry out the numerical simulations. The marked angles and designations are described in the text.

(iii) The EW for each mock quasar was estimated such that EW = EW$_*/\epsilon(\theta)$, and this process was repeated to build up a mock sample of 10^7 objects.

(iv) The difference between the mean EW of the non-BAL and BAL mock samples, $\Delta\mu_{\rm EW}$, was recorded for each geometry.

The results of this experiment are presented in Fig. 4, where we show $\Delta\mu_{\rm EW}$ as a function of $\theta_{\rm b}$ for three different values of $\Delta\theta$. Results for both normal and lognormal forms of g(EW) are shown. We also show, with a horizontal line, the *observed* value of $\Delta\mu_{\rm EW}$ for the [O III] 5007 Å emission line, while the shaded region shows the 1σ error on this value. This is the most appropriate emission line to consider, as it is forbidden and locally isotropic, but is also the most conservative, as all the other emission lines considered have negative values of $\Delta\mu_{\rm EW}$ with a smaller error. On the same plot, we also show f', which is given by

$$f' = \frac{\Omega_{\rm BAL}}{\Omega_{\rm Q}} = \frac{\int_{\theta_1}^{\theta_2} {\rm d}\Omega}{\int_{0}^{\theta_2} {\rm d}\Omega}, \quad (3)$$

where $\Omega_{\rm BAL}$ is the BALQ covering factor and $\Omega_{\rm Q}$ is the total quasar covering factor. This illustrates how the intrinsic BAL fraction depends on the outflow geometry, although it ignores flux selection effects (see Section 2.3).

The toy model predicts that large differences in EW should be present between BAL and non-BAL samples for equatorial outflows, with $\Delta\mu_{\rm EW} > 10$ Å expected for $\theta_{\rm b} \gtrsim 60^\circ$. In Fig. 5, we show the actual predicted histograms from the toy model for four different values of $\theta_{\rm b}$ and $\Delta\theta = 20^\circ$, with an accompanying cartoon showing the viewing angles to BALQs in each case. Noticeable differences in both the peaks and the widths of the distributions are present for equatorial models. Together, Figs 4 and 5 show that, under the assumptions of our toy model, geometries in which BALQs are viewed from similar (i.e. low) inclination angles to non-BALQs are strongly favoured.

on our conclusions. We adopt $\mu_* = 10$, $\sigma_* = 5$ for the normal distribution and $\mu_* = 1$, $\sigma_* = 0.7$ for the lognormal distribution.

In the context of geometric models, the simulations can be reconciled with observations via a number of possible scenarios linked to the assumptions made, namely:

(i) BALQs are viewed from angles comparable to non-BALQs, that is, low inclinations.

(ii) For reasons that are unclear, quasar disc emission is roughly isotropic, that is, $\epsilon(\theta) \sim 1$.

(iii) The line emission is strongly anisotropic in the same fashion as the continuum, that is, $\epsilon_{\rm line}(\theta) \sim \epsilon(\theta)$.

(iv) Other factors, such as obscuration or selection effects in the sample, are hiding the expected behaviour.

Clearly, a combination of two or more of these effects is also plausible. These scenarios are explored further in the remaining sections.

2.3 The effect of flux limits

In the above procedure, inclinations are generated isotropically, so the probability of a given observer orientation is simply proportional to solid angle. In reality, an anisotropic continuum source will cause substantial bias towards low-inclination sources in flux-limited samples. The effect of flux limits on the expected distributions of angles and EWs, as well as the BAL fraction, $f_{\rm BAL}$, is interesting. Imposing such a limit in the above analysis means fewer high-inclination objects with high EWs will appear in the mock sample. The value of $\Delta\mu_{\rm EW}$ will therefore decrease for a given bending angle. Furthermore, as noted by Krolik & Voit (1998), the covering factor of the outflow must dramatically increase as $\theta_{\rm b}$ increases to reproduce the observed value of $f_{\rm BAL}$.

We have conducted some preliminary tests, which show that the distribution of observer orientations in a mock sample is very sensitive to the flux limit used; the choice of flux limit to impose is thus both crucial and non-trivial. Ideally, one would reconstruct the quasar luminosity function for each geometry by deconvolving the *observed* flux distribution from the model angular distribution. Samples could then be drawn for each generated angle, corrected by $1/\epsilon(\theta)$, and then required to pass the magnitude limit of the actual sample. We reserve this process, and an investigation of the complex effects on the true value of $f_{\rm BAL}$, for a future study. Fortunately, the conclusions of this paper are not particularly sensitive to this issue, as the sharper the imposed flux cutoff, the more equatorial BAL outflows are prohibited by the model. This leads to similar conclusions to those drawn from the similarity in EW distributions: a more isotropic disc or a non-equatorial viewing angle for BALQs is favoured. The bending angle, $\theta_{\rm b}$, can thus be thought of as the flux-weighted average viewing angle – this is, after all, the angle that is really being inferred from any orientation indicator with similar selection biases to the SDSS.

3 DISCUSSION

We have demonstrated that the EW distributions of the emission lines in BAL and non-BALQs are not consistent with a model in which BALQs are viewed from equatorial angles and the continuum emission originates from an optically thick, geometrically thin accretion disc. A number of simplifications were made in the models presented in Section 2.2: the full effects of both general relativity (GR) and frequency-dependent opacities in the disc were ignored, emission line isotropy was assumed and there was no modelling of obscuration of the continuum source. We therefore now discuss the potential impact of each of these effects. We generally focus on the

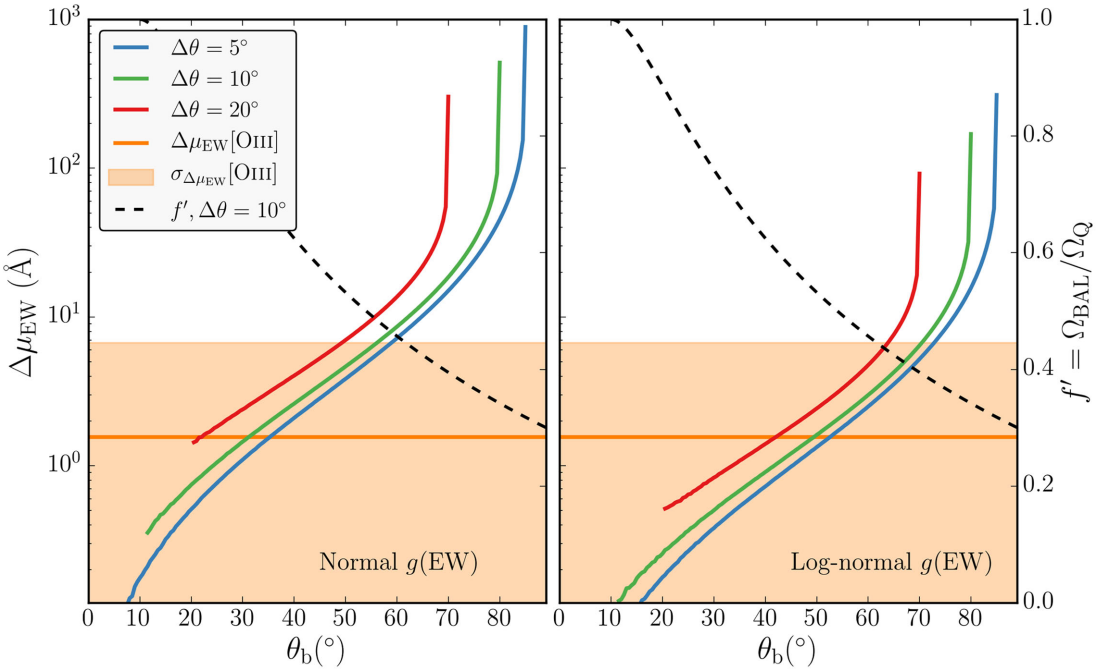

Figure 4. The results of the numerical simulation described in Section 2.2, showing difference in the mean EW of the non-BAL and BAL mock samples, $\Delta\mu_{\rm EW}$, as a function of the bending angle, $\theta_{\rm b}$. Results are shown for three different outflow covering factors ($\Delta\theta = 5°$, $10°$, $20°$) and for normal (left) and lognormal (right) forms of g(EW). The normal distribution has $\mu_* = 10$, $\sigma_* = 5$ and the lognormal distribution has $\mu_* = 1$, $\sigma_* = 0.7$. The orange horizontal line shows the observed value of $\Delta\mu_{\rm EW} = 1.56$ for the [O III] 5007 Å emission line, while the shaded region shows the 1σ error (± 5.16) on that value – note that the error extends to negative values, which cannot be shown on these axes. The dashed black line, plotted on a different axis, shows the ratio of the outflow covering factor ($\theta_1 \rightarrow \theta_2$) to the total quasar covering factor ($0 \rightarrow \theta_2$) for $\Delta\theta = 10°$.

distribution of EW[O III], as it is the most reliably isotropic line, but do devote some time also to discussing the broad emission lines (C IV 1550 Å, C III] 1909 Å and Mg II 2800 Å).

3.1 The angular distribution of emission from an accretion disc

The most widely used theoretical model for thin accretion discs is the so-called α-disc model of Shakura & Sunyaev (1973). There are a number of well-documented problems when fitting AGN spectra with thin disc models (e.g. Koratkar & Blaes 1999; Antonucci 2013; Shankar et al. 2016). Despite these problems, Capellupo et al. (2015) succeeded in fitting α-disc models to AGN spectra when the effects of GR, mass-loss and Comptonization were included. In this section, we start by discussing the angular distribution of emission from a classic α-disc, before exploring opacity and GR effects. In order to do so, we use AGNSPEC (Hubeny et al. 2000; Davis & Hubeny 2006; Davis, Woo & Blaes 2007). We stress that the discussion here is not limited to α-discs; the only real condition for the angular distributions derived here is that the disc is geometrically thin and optically thick.

Any geometrically thin, optically thick disc will appear foreshortened and limb darkened (if temperature decreases with height from the central disc plane). Foreshortening is a simple $\cos\theta$ geometric effect. Limb darkening, $\eta(\theta)$, is usually approximated by a linear dependence of the emergent flux on $\cos\theta$, that is,

$$\eta(\theta) = a\,(1 + b\cos\theta), \tag{4}$$

where a is a normalization constant and b governs the strength of the limb darkening. Setting $b = 3/2$ tends to give good agreement with solar observations (e.g. Mihalas 1978). In reality, limb darkening is not frequency independent and depends on the bound–free and bound–bound opacities in the disc. In addition, it has been shown that GR light bending can 'isotropize' the radiation field in XRBs (Zhang, Cui & Chen 1997; Muñoz-Darias et al. 2013), in some cases overcoming foreshortening effects.

In order to assess the impact of GR and disc opacities on $\epsilon(\theta)$, we use AGNSPEC models. AGNSPEC works by first conducting a stellar atmosphere calculation to obtain the SED from a series of annuli, before using KERRTRANS (Agol 1997) to calculate the emergent SED by ray tracing along Kerr geodesics. Fig. 6 shows $\epsilon(\theta)$ as a function of θ for two AGNSPEC models for minimally and maximally spinning BHs. The models are characterized by $M_{\rm BH} = 10^9\,{\rm M}_\odot$ and an Eddington fraction of 0.2. The angular distribution is fairly insensitive to these choices. For comparison, we also show foreshortened and limb-darkened predictions for SS73 models. Although the AGNSPEC continua are significantly more isotropic at 500 Å, there is very little effect redward of around 1000 Å, which is the relevant region of $\epsilon(\theta)$ for [O III] 5007 Å, C IV 1550 Å, C III] 1909 Å and Mg II 2800 Å. In fact, using the foreshortened estimate is the conservative (least anisotropic) prescription in these regimes. This therefore justifies the form of $\epsilon(\theta)$ used in the toy models and demonstrates that GR does not affect the shapes of the emission line EW distributions in the UV and optical regimes.

3.2 Obscuration

Differential obscuration of the continuum source and line-emitting region by a dusty torus or other circumnuclear absorber can change the observed EW. Caccianiga & Severgnini (2011, hereafter C11) showed that the distribution of EW[O III] can also be well fitted by an obscuration model. They find that AGNs with column

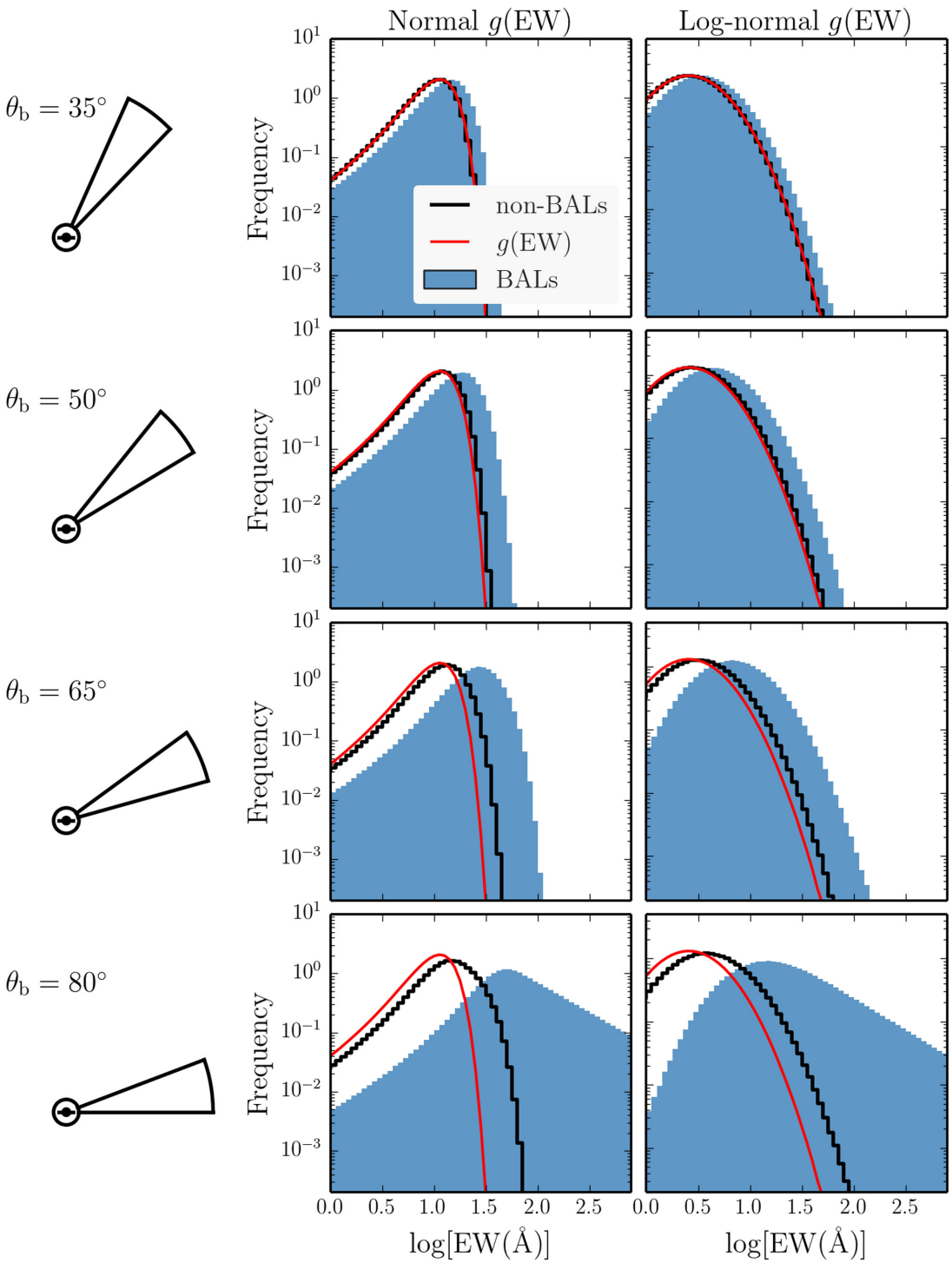

Figure 5. Normalized histograms of mock EWs for BAL and non-BALQs from the toy model described in Section 2.2, for four different values of θ_b and $\Delta\theta = 20°$. The intrinsic 'face-on' distribution used as input, g(EW), is shown in red in each case and the BAL and non-BAL mock quasar samples are shown in the same corresponding colours as for the real data in Fig. 2. The normal g(EW) distribution has $\mu_* = 10$, $\sigma_* = 5$ and the lognormal distribution has $\mu_* = 1$, $\sigma_* = 0.7$.

densities of $N_H \gtrsim 10^{22}$ cm^{-2} can explain the high EW power-law tail. BALQs exhibit strong X-ray absorption with column densities of $N_H \sim 10^{22-24}$ cm^{-2} (Green & Mathur 1996; Gallagher et al. 1999; Mathur et al. 2000; Green et al. 2001; Grupe, Mathur & Elvis 2003; Morabito et al. 2014). This places BALQs firmly in the EW tail according to the C11 model. Of course, only LOBALQs had EW[O III] measurements in the sample used here, but these generally show even higher column densities, approaching Compton-thick values (Morabito et al. 2011).

We therefore suggest that the obscuration model of C11 cannot explain the EW[O III] distribution of LoBALQs. The similarity of the observed LoBAL and non-BAL distributions also means that

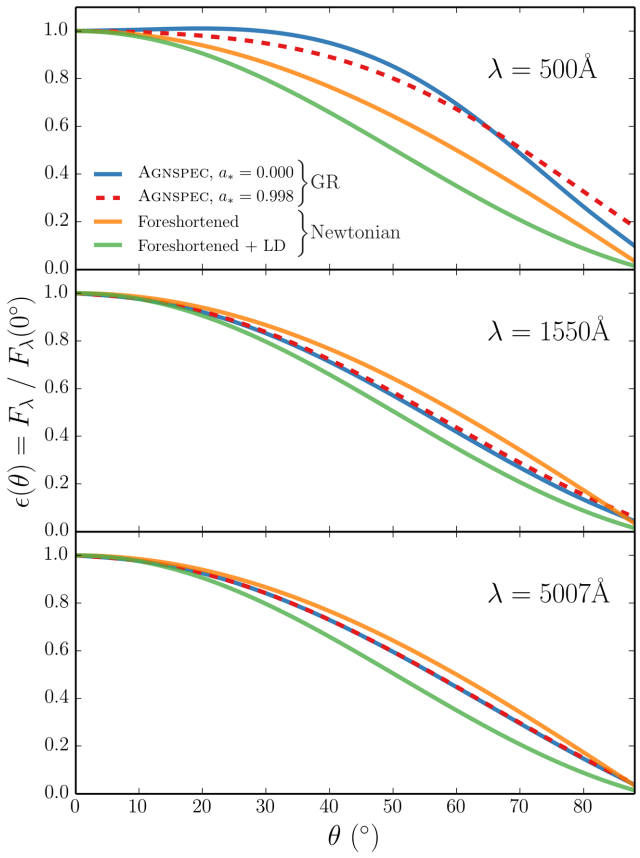

Figure 6. Angular variation of continuum luminosity from AGNSPEC and classical thin disc models. The monochromatic continuum luminosities is divided by the monochromatic continuum luminosity at 10°, from AGNSPEC and classical thin disc models, at three different wavelengths. The models are computed for an Eddington fraction of 0.2 and $M_{\rm BH} = 10^9 {\rm M}_\odot$. In each panel, we show both Kerr and Schwarzschild AGNSPEC models, and the classical models are for both pure foreshortened discs and foreshortened and limb-darkened (LD) discs.

obscuration is unlikely to drive the behaviour of EW[O III] as a whole. These conclusions are moderated if the line of sight to the X-ray source, which determines the measured $N_{\rm H}$, experiences a different absorbing column to that of the optical continuum. They are also dependent on the particular absorption model used by C11. Indeed, it is worth noting at this point that there is a degree of scatter in the $N_{\rm H}$ values measured from X-ray and optical observations (Maiolino et al. 2001a; Maiolino, Marconi & Oliva 2001b), as could be produced by differing viewing angles to the X-ray and optical radiation sources. Further work is clearly needed, but considering the absorption properties of BALQs strengthens the findings presented in Section 2.

3.3 Line anisotropy

Optically thin lines are isotropic – the *local* escape probabilities in each direction are equal due to the low optical depth. Anisotropy can however be introduced into optically thin line emission by variation in continuum absorption. Indeed, Kraemer et al. (2011) showed that the strength of [O III] 5007 Å compared to the infrared [OIV] 28.59 μm line varies between type 1 and type 2 AGNs. However, this variation is due to frequency-dependent absorption, and so should not affect the distribution of EW[O III]. If a higher continuum optical depth was experienced along the line of sight to the NLR than to the continuum source, then this could mask EW trends, but this is the opposite behaviour to that expected from type 1/type 2 unification geometries.

When lines are optically thick, the situation is more complex, as local velocity gradients then determine their anisotropy. Keplerian velocity shear has been shown to modify the shape of disc-formed emission lines (Horne & Marsh 1986), whilst an additional radial shear from a wind can cause double-peaked lines to become single peaked (Murray & Chiang 1996, 1997; Flohic, Eracleous & Bogdanović 2012). Although there is a sub-population of AGNs with double-peaked lines (e.g. Eracleous & Halpern 1994, 2003), this fraction is only around 3 per cent (Strateva et al. 2003), so AGN and quasar spectra in general show broad, single-peaked lines. The single-peaked nature of most quasar emission lines implies that they are not formed in a Keplerian disc, that quasars are mostly viewed pole-on, that radial velocity gradients modify the profile shapes or that an additional single-peaked component is required (Storchi-Bergmann et al. 2017). Disc-shaped BLRs are popular in the literature (e.g. Decarli et al. 2008; Gaskell & Goosmann 2013; Begelman & Silk 2016) and are commonly invoked to explain reverberation mapping results (Pozo Nuñez et al. 2013; Goad & Korista 2014; Pancoast, Brewer & Treu 2014a; Pancoast et al. 2014b). Furthermore, R11 suggested that the broad emission lines form in a disc and trace the disc emission in terms of their anisotropy. If this was the case, we would not expect a difference in the BAL and non-BALQ EW distributions. However, an emission line is only purely foreshortened if formed in a disc with zero velocity shear or an isotropic local velocity gradient. Neither of these scenarios is particularly plausible.

We have explored the expected angular distributions of line emissivity if the lines came from a region subject to Keplerian velocity shear. A more detailed discussion is found in Appendix A. The results show that optically thick line emission from a Keplerian disc does not follow a $\cos\theta$ distribution unless $H/R \sim 0.01$, which is unrealistically small for the BLR (Kollatschny & Zetzl 2013; Pancoast et al. 2014b). Thus, a *Keplerian* disc-like BLR cannot explain the overall EW distributions of the broad emission lines or the similarity of the distributions of C IV 1550 Å EW and Mg II 2800 Å EW in BAL and non-BALQs. The presence of an equatorial wind would exacerbate the effect and cause more line emission to escape along the radial velocity gradient towards high inclinations. Other models, in which the BLR is made up of a series of clouds orbiting in a disc-shaped structure (see Sulentic, Marziani & Dultzin-Hacyan 2000a, for a review), could feasibly produce a $\cos\theta$ angular dependence. In this case, local line emission is isotropic but is then affected by continuum opacity from other orbiting clouds. Radiative transfer effects within the cloud could also lead to more complex line anisotropy effects (Davidson & Netzer 1979; Ferland et al. 1992; Korista et al. 1997). We cannot exclude such a model but argue that, as line anisotropy cannot significantly affect the distribution of EW[O III], it is also unlikely to significantly affect even the EW of lines formed in the BLR from permitted dipole transitions.

4 CLUES FROM OTHER SOURCES

Having explored the behaviour of emission line EW as a potential orientation indicator, we now devote some time to discussing other observables that might trace viewing angles to BAL and non-BALQs. We will also briefly discuss the constraints from theoretical work and the potential implications for the wind-driving mechanism.

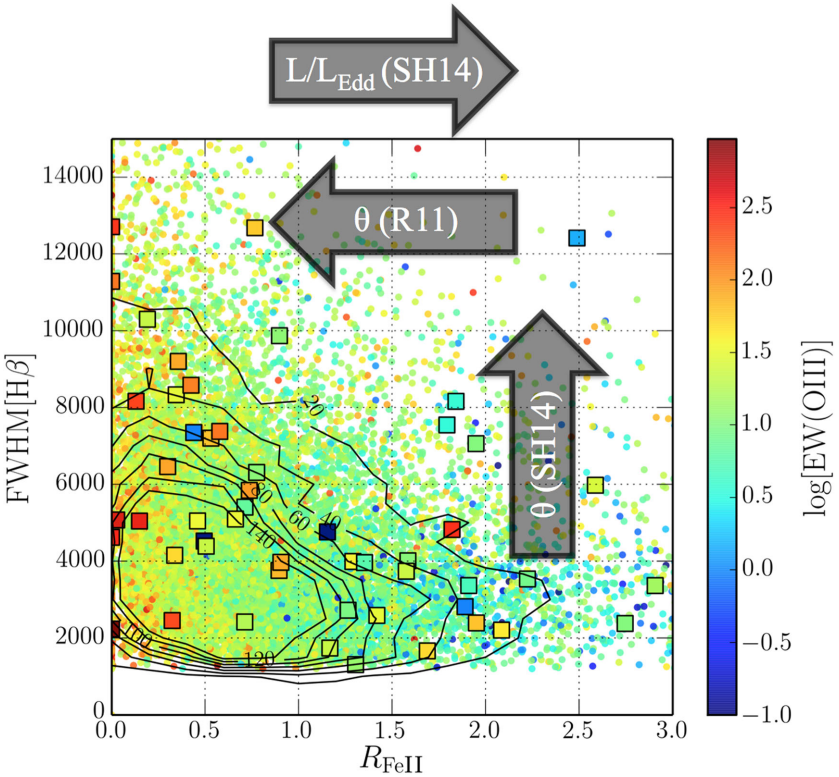

Figure 7. EV1 for LoBAL and non-BALQs. Full width at half maximum (FWHM) of the Hβ line plotted against the relative iron strength, $R_{\rm Fe\,II}$. The colour coding corresponds to EW[O III]. The dots mark all quasars from sample A, while the squares mark those with Mg II LoBALs. A few of the Mg II LoBALQs are missing due to their lack of FWHM[Hβ] measurements. The arrows show the approximate direction of the expected trend with increasing inclination (θ) under both the SH14 and R11 interpretations, and the expected trend with an increasing Eddington fraction ($L/L_{\rm Edd}$) from SH14 only. HiBAL quasars cannot be placed on this plot due to the lack of rest-frame optical coverage.

4.1 Eigenvector 1

EV1 is a fundamental parameter space for AGNs and quasars (Boroson & Green 1992; Sulentic et al. 2000b; Marziani et al. 2001; Shen & Ho 2014). It relates the FWHM of Hβ, the relative iron strength, $R_{\rm Fe\,II}$, and EW[O III]. Both EW[O III] and FWHM[Hβ] have been used as orientation indicators: FWHM[Hβ] should increase with inclination if the line formation region is at all disc shaped due to velocity projection effects. This means that comparing the LoBALQ EV1 distribution to the non-BALQ EV1 distribution is particularly interesting. Once again, the SDSS HiBALQs cannot be placed in this space due to the lack of rest-frame optical coverage.

Fig. 7 shows the quasar distribution from sample A in the EV1 parameter space, with LOBALQs from sample A overplotted. Shen & Ho (2014, hereafter SH14) propose that the main inclination driver in this parameter space is FWHM[Hβ]and that high-inclination sources should thus cluster nearer to the top of the plot. In contrast, R11's analysis predicts that high-inclination sources should cluster around high EW[O III]. As EW[O III] and FWHM[Hβ] are very weakly correlated (Spearman's rank coefficient of 0.14), this means they should lie to the left of the parameter space, due to the clear correlation between EW[O III] and $R_{\rm Fe\,II}$. These expected trends are shown with arrows in Fig. 7; inspection of the figure clearly shows that LOBALQs are not confined to one region of the EV1 parameter space. This is contrary to previous findings with different samples in which LOBALQs were thought to lie at extreme ends due to low EW[O III] and high $R_{\rm Fe\,II}$ (Boroson & Meyers 1992; Turnshek et al. 1997; Runnoe et al. 2014).

In order to assess this more quantitatively, we also show contours of quasar counts overlaid on the scatter plot. The contours correspond to the number of objects in each bin, where the bins are of size $\Delta R_{\rm Fe\,II} = 0.2$ and ΔFWHM[Hβ] = 500 km s^{-1}. The percentage of quasars falling within the inner contour is 45 per cent, whereas only 18 per cent of LoBALQs fall in the space. Conversely, 24 per cent of LoBALQs fall outside the outermost contour compared to 10 per cent of non-BALQs. It would therefore appear that BALQs are slightly preferentially clustered towards the high-mass and high-inclination end of the EV1 space (under the interpretation of SH14). This is further illustrated by Fig. 8, which shows the LoBAL fraction in larger bins compared to the mean LoBAL fraction. This is again suggestive of an overdensity of LoBALQs towards the upper right of the parameter space. It is also clear that a unification picture in which BALQs are viewed exclusively from high inclinations is inconsistent with both the R11 and the SH14 interpretations of the EV1 parameter space.

Larger data sets, preferably including HiBAL quasars with EV1 measurements, are needed in order to properly constrain the EV1 behaviour of BALQs. However, overall, the behaviour of EV1 in LoBALQs slightly strengthens the conclusion that BALQs are not viewed exclusively from extreme inclinations, or alternatively, that we do not yet understand the real drivers of EV1.

4.2 Polarization

Spectropolarimetry of BALQs offers some of the best insights into the geometries of BAL outflows and tends to show a few key

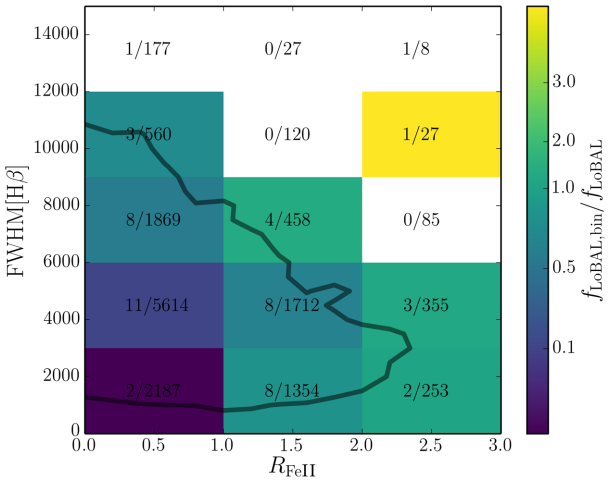

Figure 8. LoBAL fraction compared to global LoBAL fraction in the EV1 space, in bins of $\Delta R_{\rm Fe\,II} = 1$ and $\Delta{\rm FWHM[H}\beta] = 3000\,{\rm km\,s^{-1}}$. The contour shows the outermost contour from Fig. 7 for reference. The text shows $N_{\rm LoBAL}/N_{\rm non\text{-}BAL}$, where $N_{\rm LoBAL}$ is the number of LoBALQs in the bin and $N_{\rm non\text{-}BAL}$ in the number of non-BALQs in the bin.

properties. The first is enhanced polarization in the BAL troughs themselves (Ogle et al. 1999; Schmidt & Hines 1999). This is readily explained by a scattering region unobscured by the BAL trough, with the higher polarization percentage simply due to the decreased direct flux. The second property is a continuum polarization percentage in BALQs that is around two times greater, on average, than seen in the non-BAL population (Schmidt & Hines 1999). A histogram of the continuum polarization percentages of a sample of BALQs from Schmidt & Hines (1999) is compared to the type 1 and type 2 AGN populations from Marin (2014) in the left-hand panel of Fig. 9. The corresponding cumulative distribution function is shown in the right-hand panel. These show that BAL polarization percentages lie between those of type 1 and type 2 AGNs. If type 1 and type 2 objects are viewed from low and high inclinations, respectively, as expected from unified models, this implies intermediate inclinations for BALQs.

The third characteristic polarization property of BALQs is a polarization angle with respect to the radio axis, ΔPA of $\gtrsim 60^\circ$ in RL objects, as found in all of the seven BALQ measurements compiled by Brotherton et al. (2006). These observations have been explained by a model with a polar scattering region, distinct from the BLR and BAL regions, which is then viewed at an equatorial angle (e.g. Cohen et al. 1995; Goodrich & Miller 1995; Lamy & Hutsemékers 2004). However, large values of ΔPA can be produced at intermediate viewing angles of around 45° (Kartje 1995; Smith et al. 2004; Axon et al. 2008; Borguet et al. 2011). We suggest that polarization predictions similar to those described by Marin & Goosmann (2013) are carried out for full radiative transfer wind models (e.g. Matthews et al. 2016). Overall, however, quasar polarization properties imply that BALQs are viewed from higher than average, intermediate viewing angles between type 1 and 2 AGNs.

4.3 Radio properties

Radio measurements have long been proposed as a potential probe of the quasar orientation (Orr & Browne 1982). In particular, measurements of jet Lorentz factors, radio spectral index and the ratio of the core flux to extended flux, the so-called radio core dominance, log R, offer ways to measure radio jet inclination. Although they are preferentially radio quiet (Stocke et al. 1992; Brotherton et al. 1998; Shankar, Dai & Sivakoff 2008), radio observations of BALQs offer some of the strongest evidence against equatorial geometric models: for one, they have led to the discovery of the (aforementioned) polar BALQs (Zhou et al. 2006; Ghosh & Punsly 2007; Berrington et al. 2013). While there is evidence that BALQs generally possess steeper spectral indices (DiPompeo et al. 2011; Bruni et al. 2012), the range of values is indicative of a variety of viewing angles (Becker et al. 2000; Montenegro-Montes et al. 2008; DiPompeo et al. 2012). In addition, at high-redshift, Tuccillo et al. (2017) found statistically similar spectral index distributions in BAL and non-BAL quasars.

Recent long baseline radio observations of BALQs found very compact (<10 pc) radio structure, suggestive of a young radio source (Doi et al. 2013; Kunert-Bajraszewska et al. 2015),

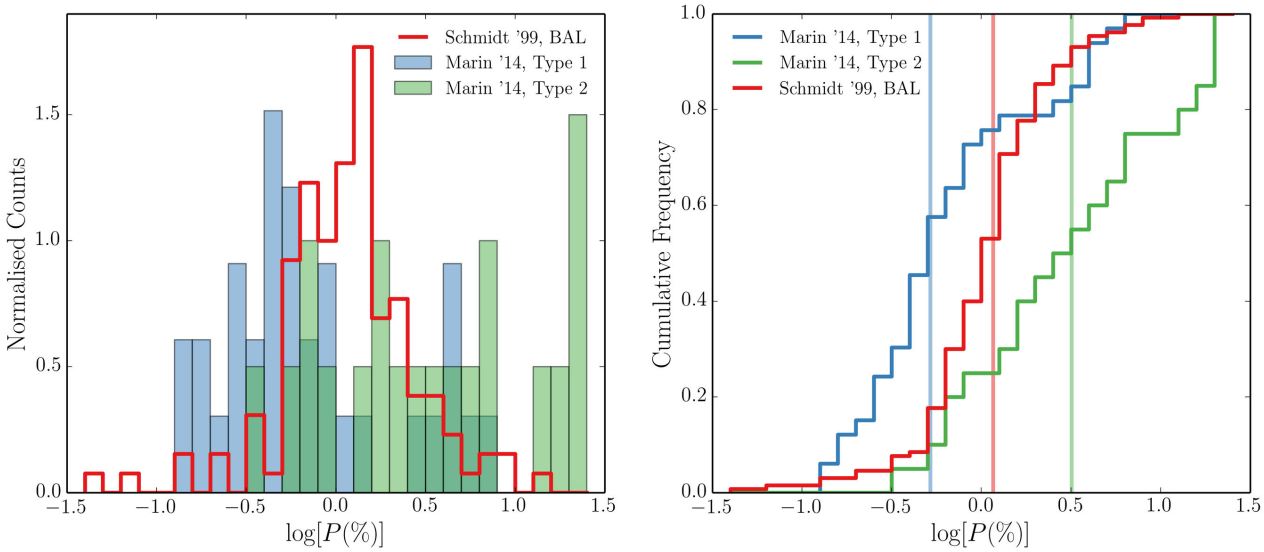

Figure 9. Left: histograms of polarization percentages for BALQs from Schmidt & Hines (1999) together with the Marin (2014) AGN sample. Right: cumulative distribution functions of the histograms shown in the left-hand panel, with the same colour-coding and x-axis scale. The translucent vertical lines mark the median value in each sample.

although orientation is also thought to have a role (Cegłowski, Kunert-Bajraszewska & Roskowiński 2015). The similarity in UV properties means that many of the conclusions drawn from RL samples should also be applicable to radio-quiet BALQs (Rochais et al. 2014). Overall, radio studies of BALQs imply that they are viewed from a range of angles but higher than average, as suggested by, e.g. DiPompeo et al. (2011). Neither evolutionary or geometric models can adequately account for the global radio properties of BALQs (see Doi et al. 2013, for a good discussion).

4.4 Theory of winds

Theoretical predictions for outflow geometries depend on the driving mechanism being considered. Two of the most promising ways for BAL outflows to be launched are via the magnetocentrifugal 'bead on a wire' mechanism (Blandford & Payne 1982) or radiation pressure on spectral lines ('line-driving'). Given the lack of knowledge about the magnetic field in quasar accretion discs, theoretical considerations provide very few constraints in the case of magnetocentrifugal outflows. Tests of the Emmering, Blandford & Shlosman (1992) model, in which a magnetohydrodynamic wind produces the broad emission lines, favour launching angles of $\gtrsim 30^{\circ}$ in order to match observed linewidths (Chajet & Hall 2013, 2017). However, the exact relationship between such a wind and BAL outflows is not clear.

We know line-driving is present in many quasar outflows, thanks to the discovery of line-locking signatures (Arav et al. 1995; Arav 1996; North, Knigge & Goad 2006; Bowler et al. 2014; but see also Cottis et al. 2010). Hydrodynamic simulations have been successful in producing substantial line-driven disc winds (Proga et al. 2000; Proga & Kallman 2004). Although these models generally favour equatorial flows, the ionization state is crucial in determining the degree of collimation and depends on disc and X-ray luminosities as well as black hole mass (Proga, Stone & Drew 1998; Proga & Kallman 2004). The level of shielding (Murray et al. 1995; Proga & Kallman 2004) and clumping (e.g. Junkkarinen, Burbidge & Smith 1983; Weymann, Turnshek & Christiansen 1985; Hamann et al. 2013; Matthews et al. 2016) may also be important. Fully coupled radiative transfer and hydrodynamic simulations are important in this regard, as they properly account for the radiation field (Sim et al. 2012; Higginbottom et al. 2014).

5 CONCLUSIONS

We have explored the emission line properties of BAL and non-BALQs, particularly focusing on the EW distributions in two redshift ranges of the SDSS quasar catalogue. Our main conclusion is that the EW distributions of BAL and non-BALQs are remarkably similar and that this is *not* what one would expect from a unification model in which an equatorial BAL outflow rises from a foreshortened accretion disc. This geometry is widely used in geometric unification and BAL outflow models (e.g. de Kool & Begelman 1995; Murray et al. 1995; Elvis 2000; Proga et al. 2000; Proga & Kallman 2004; Borguet & Hutsemékers 2010; Risaliti & Elvis 2010; Higginbottom et al. 2013; Nomura et al. 2013, 2016).

In order to calculate the expected distributions from different wind geometries, we conducted a series of simulations similar to those described by R11. As expected, these simulations confirmed the above finding, predicting differences of >10Å in the mean EW for $\theta_{\rm b} \gtrsim 60^{\circ}$ – differences that are not seen in the data. We demonstrated that GR or opacity effects in the disc do not cause the continuum to become more isotropic in the relevant wavelength regimes. Line anisotropy and obscuration cannot effectively hide the expected inclination trend – in fact, the column density measurements from X-ray observations of BALQs suggest that obscuration does not drive the distribution of EW[O III].

There are three basic ways to explain our results.

(i) *Scenario A:* quasar discs radiate anisotropically, as expected from a geometrically thin, optically thick accretion disc. In this case, BAL outflows cannot only emerge at extreme inclinations and should instead be seen from low to intermediate inclinations.

(ii) *Scenario B:* the quasar continuum is much more isotropic than one would expect from a geometrically thin, optically thick accretion disc.

(iii) *Scenario C:* the geometric unification model does not explain the incidence of BALs in quasars, or requires an additional component which is *time dependent*, such as an evolutionary or accretion state origin for BAL outflows. If this is the case, the wind must still have a geometry, which is important to constrain in order to understand the driving mechanism and estimate the feedback efficiency.

We then examined the relative merits of these scenarios in the context of the large body of work on quasar orientation and BALQs. Based on the polarization and radio properties, a scenario in which BAL outflows emerge at intermediate inclinations between type 1 and type 2 AGNs is favoured. It is still possible that the actual outflow has a wide covering factor, but lower inclination quasars appear preferentially in flux-limited samples due to the effect of foreshortening and continuum absorption. We recommend that future radiative transfer modelling efforts explore different outflow geometries and that detailed polarization modelling is undertaken to constrain the outflow opening angles. We note that the current benchmark line-driven wind models produce equatorial flows (see Section 4.4) – a picture that is in tension with our results.

We also suggest that the accretion disc physics is a crucial aspect to understand, particularly if equatorial winds are indeed present. We cannot distinguish more effectively between the above scenarios until the continuum source in AGN is understood. We point to the so-called accretion-disc size problem (e.g. Morgan et al. 2010; Edelson et al. 2015) as one of many results that indicate further problems when reconciling thin disc quasar models with observations. We hope that a 'two birds, one stone' scenario may arise that explains some of the observed discrepancies simultaneously. If nothing else, our work adds to the evidence that many simple unification models are not sufficient to describe the diverse phenomenology of AGNs and quasars.

ACKNOWLEDGEMENTS

The work of JHM is funded by the Science and Technology Facilities Council (STFC), via a studentship whilst at Southampton and a consolidated grant at Oxford. The work of CK is also supported by the STFC and a Leverhulme fellowship. KSL acknowledges the support of NASA for this work through grant NNG15PP48P to serve as a science adviser to the Astro-H project. We would like to thank the anonymous referee for a constructive and insightful report that improved the quality of the paper. JHM would particularly like to thank Lance Miller and Poshak Gandhi for being such wonderful PhD examiners. More generally, we would like to thank Omer Blaes, Ivan Hubeny and Shane Davis for their help with AGNSPECand Mike Brotherton, Mike DiPompeo and Frederic Marin for their correspondence regarding polarization measurements and orientation indicators. We are also grateful to Stuart Sim, Nick

Higginbotton, Sam Mangham, Francesco Shankar, Daniel Proga, Leah Morabito, Rob Fender, Tony Bell, Katherine Blundell, Will Potter, Sam Connolly and Sebastien Hoenig for useful discussions. Figures were produced using the `matplotlib` plotting library (Hunter 2007). This work made use of the Sloan Digital Sky Survey. Funding for the Sloan Digital Sky Survey has been provided by the Alfred P. Sloan Foundation, the US Department of Energy Office of Science and the Participating Institutions.

REFERENCES

Abazajian K. N. et al., 2009, ApJS, 182, 543
Agol E., 1997, PhD thesis, Univ. California
Albareti F. D. et al., 2015, MNRAS, 452, 4153
Alexandroff R. et al., 2013, MNRAS, 435, 3306
Allen J. T., Hewett P. C., Maddox N., Richards G. T., Belokurov V., 2011, MNRAS, 410, 860
Antonucci R., 2013, Nature, 495, 165
Antonucci R. R. J., Miller J. S., 1985, ApJ, 297, 621
Arav N., 1996, ApJ, 465, 617
Arav N., Korista K. T., Barlow T. A., Begelman, 1995, Nature, 376, 576
Axon D. J., Robinson A., Young S., Smith J. E., Hough J. H., 2008, Mem. Soc. Astron. Ital., 79, 1213
Baskin A., Laor A., 2005, MNRAS, 358, 1043
Becker R. H., White R. L., Gregg M. D., Brotherton M. S., Laurent-Muehleisen S. A., Arav N., 2000, ApJ, 538, 72
Begelman M. C., Silk J., 2016, MNRAS, preprint (arXiv:e-print)
Berrington R. C. et al., 2013, MNRAS, 436, 3321
Bhatia A. K., Kastner S. O., 1992, ApJS, 79, 139
Blandford R. D., Payne D. G., 1982, MNRAS, 199, 883
Borguet B., Hutsemékers D., 2010, A&A, 515, A22
Borguet B., Hutsemékers D., Letawe G., Letawe Y., Magain P., 2011, in Bastien P., Manset N., Clemens D. P., St-Louis N., eds, ASP Conf. Ser. Vol. 449, Astronomical Polarimetry 2008: Science from Small to Large Telescopes. Astron. Soc. Pac., San Francisco, p. 459
Boroson T. A., Green R. F., 1992, ApJS, 80, 109
Boroson T. A., Meyers K. A., 1992, ApJ, 397, 442
Bowler R. A. A., Hewett P. C., Allen J. T., Ferland G. J., 2014, MNRAS, 445, 359
Brotherton M. S., van Breugel W., Smith R. J., Boyle B. J., Shanks T., Croom S. M., Miller L., Becker R. H., 1998, ApJ, 505, L7
Brotherton M. S., De Breuck C., Schaefer J. J., 2006, MNRAS, 372, L58
Bruni G. et al., 2012, A&A, 542, A13
Caccianiga A., Severgnini P., 2011, MNRAS, 415, 1928 (C11)
Capellupo D. M., Netzer H., Lira P., Trakhtenbrot B., Mejía-Restrepo J., 2015, MNRAS, 446, 3427
Cegłowski M., Kunert-Bajraszewska M., Roskowiński C., 2015, MNRAS, 450, 1123
Chajet L. S., Hall P. B., 2013, MNRAS, 429, 3214
Chajet L. S., Hall P. B., 2017, MNRAS, 465, 1741
Cohen M. H., Ogle P. M., Tran H. D., Vermeulen R. C., Miller J. S., Goodrich R. W., Martel A. R., 1995, ApJ, 448, L77
Cottis C. E., Goad M. R., Knigge C., Scaringi S., 2010, MNRAS, 406, 2094
Davidson K., Netzer H., 1979, Rev. Mod. Phys., 51, 715
Davis S. W., Hubeny I., 2006, ApJS, 164, 530
Davis S. W., Woo J.-H., Blaes O. M., 2007, ApJ, 668, 682
de Kool M., Begelman M. C., 1995, ApJ, 455, 448
Decarli R., Labita M., Treves A., Falomo R., 2008, MNRAS, 387, 1237
DiPompeo M. A., Brotherton M. S., De Breuck C., Laurent-Muehleisen S., 2011, ApJ, 743, 71
DiPompeo M. A., Brotherton M. S., Cales S. L., Runnoe J. C., 2012, MNRAS, 427, 1135
Doi A. et al., 2013, PASJ, 65, 57
Echevarria J., 1988, MNRAS, 233, 513
Edelson R. et al., 2015, ApJ, 806, 129
Elvis M., 2000, ApJ, 545, 63
Emmering R. T., Blandford R. D., Shlosman I., 1992, ApJ, 385, 460
Eracleous M., Halpern J. P., 1994, ApJS, 90, 1
Eracleous M., Halpern J. P., 2003, ApJ, 599, 886
Farrah D., Lacy M., Priddey R., Borys C., Afonso J., 2007, ApJ, 662, L59
Ferland G. J., Peterson B. M., Horne K., Welsh W. F., Nahar S. N., 1992, ApJ, 387, 95
Flohic H. M. L. G., Eracleous M., Bogdanović T., 2012, ApJ, 753, 133
Gallagher S. C., Brandt W. N., Sambruna R. M., Mathur S., Yamasaki N., 1999, ApJ, 519, 549
Gaskell C. M., Goosmann R. W., 2013, ApJ, 769, 30
Ghosh K. K., Punsly B., 2007, ApJ, 661, L139
Goad M. R., Korista K. T., 2014, MNRAS, 444, 43
Goodrich R. W., Miller J. S., 1995, ApJ, 448, L73
Green P. J., Mathur S., 1996, ApJ, 462, 637
Green P. J., Aldcroft T. L., Mathur S., Wilkes B. J., Elvis M., 2001, ApJ, 558, 109
Gregg M. D., Becker R. H., Brotherton M. S., Laurent-Muehleisen S. A., Lacy M., White R. L., 2000, ApJ, 544, 142
Gregg M. D., Becker R. H., de Vries W., 2006, ApJ, 641, 210
Grupe D., Mathur S., Elvis M., 2003, AJ, 126, 1159
Hamann F., Chartas G., McGraw S., Rodriguez Hidalgo P., Shields J., Capellupo D., Charlton J., Eracleous M., 2013, MNRAS, 435, 133
Herter T., Lacasse M. G., Wesemael F., Winget D. E., 1979, ApJS, 39, 513
Hessman F. V., Robinson E. L., Nather R. E., Zhang E.-H., 1984, ApJ, 286, 747
Higginbottom N., Knigge C., Long K. S., Sim S. A., Matthews J. H., 2013, MNRAS, 436, 1390
Higginbottom N., Proga D., Knigge C., Long K. S., Matthews J. H., Sim S. A., 2014, ApJ, 789, 19
Horne K., Marsh T. R., 1986, MNRAS, 218, 761
Hubeny I., Agol E., Blaes O., Krolik J. H., 2000, ApJ, 533, 710
Hunter J. D., 2007, Comput. Sci. Eng., 9, 90
Junkkarinen V. T., Burbidge E. M., Smith H. E., 1983, ApJ, 265, 51
Kartje J. F., 1995, ApJ, 452, 565
Knigge C., Scaringi S., Goad M. R., Cottis C. E., 2008, MNRAS, 386, 1426
Kollatschny W., Zetzl M., 2013, A&A, 558, A26
Koratkar A., Blaes O., 1999, PASP, 111, 1
Korista K., Baldwin J., Ferland G., Verner D., 1997, ApJS, 108, 401
Kraemer S. B., Schmitt H. R., Crenshaw D. M., Meléndez M., Turner T. J., Guainazzi M., Mushotzky R. F., 2011, ApJ, 727, 130
Krolik J. H., Voit G. M., 1998, ApJ, 497, L5
Kunert-Bajraszewska M., Cegłowski M., Katarzyński K., Roskowiński C., 2015, A&A, 579, A109
Lamy H., Hutsemékers D., 2004, A&A, 427, 107
Laor A., Netzer H., 1989, MNRAS, 238, 897
Lipari S. et al., 2009, MNRAS, 392, 1295
Lusso E. et al., 2012, MNRAS, 425, 623
Maiolino R., Marconi A., Salvati M., Risaliti G., Severgnini P., Oliva E., La Franca F., Vanzi L., 2001a, A&A, 365, 28
Maiolino R., Marconi A., Oliva E., 2001b, A&A, 365, 37
Malkan M. A., 1983, ApJ, 268, 582
Malkan M. A., Sargent W. L. W., 1982, ApJ, 254, 22
Marin F., 2014, MNRAS, 441, 551
Marin F., 2016, MNRAS, 460, 3679
Marin F., Goosmann R. W., 2013, MNRAS, 436, 2522
Marziani P., Sulentic J. W., Zwitter T., Dultzin-Hacyan D., Calvani M., 2001, ApJ, 558, 553
Mathur S. et al., 2000, ApJ, 533, L79
Matthews J. H., Knigge C., Long K. S., Sim S. A., Higginbottom N., 2015, MNRAS, 450, 3331
Matthews J. H., Knigge C., Long K. S., Sim S. A., Higginbottom N., Mangham S. W., 2016, MNRAS, 458, 293
Mihalas D., 1978, Stellar Atmospheres, 2nd edn. Freeman & Co., San Francisco
Montenegro-Montes F. M., Mack K.-H., Vigotti M., Benn C. R., Carballo R., González-Serrano J. I., Holt J., Jiménez-Luján F., 2008, MNRAS, 388, 1853
Morabito L. K., Dai X., Leighly K. M., Sivakoff G. R., Shankar F., 2011, ApJ, 737, 46

Morabito L. K., Dai X., Leighly K. M., Sivakoff G. R., Shankar F., 2014, ApJ, 786, 58
Morgan C. W., Kochanek C. S., Morgan N. D., Falco E. E., 2010, ApJ, 712, 1129
Muñoz-Darias T., Coriat M., Plant D. S., Ponti G., Fender R. P., Dunn R. J. H., 2013, MNRAS, 432, 1330
Murray N., Chiang J., 1996, Nature, 382, 789
Murray N., Chiang J., 1997, ApJ, 474, 91
Murray N., Chiang J., Grossman S. A., Voit G. M., 1995, ApJ, 451, 498
Noebauer U. M., Long K. S., Sim S. A., Knigge C., 2010, ApJ, 719, 1932
Nomura M., Ohsuga K., Wada K., Susa H., Misawa T., 2013, PASJ, 65, 40
Nomura M., Ohsuga K., Takahashi H. R., Wada K., Yoshida T., 2016, PASJ, 68, 16
North M., Knigge C., Goad M., 2006, MNRAS, 365, 1057
Ogle P. M., Cohen M. H., Miller J. S., Tran H. D., Goodrich R. W., Martel A. R., 1999, ApJS, 125, 1
Orr M. J. L., Browne I. W. A., 1982, MNRAS, 200, 1067
Pancoast A., Brewer B. J., Treu T., 2014a, MNRAS, 445, 3055
Pancoast A., Brewer B. J., Treu T., Park D., Barth A. J., Bentz M. C., Woo J.-H., 2014b, MNRAS, 445, 3073
Pâris I. et al., 2017, A&A, 597, A79 (P16)
Patterson J., 1984, ApJS, 54, 443
Pozo Nuñez F. et al., 2013, A&A, 552, A1
Proga D., Kallman T. R., 2004, ApJ, 616, 688
Proga D., Stone J. M., Drew J. E., 1998, MNRAS, 295, 595
Proga D., Stone J. M., Kallman T. R., 2000, ApJ, 543, 686
Reichard T. A. et al., 2003, AJ, 126, 2594
Reyes R. et al., 2008, AJ, 136, 2373
Risaliti G., Elvis M., 2010, A&A, 516, A89
Risaliti G., Salvati M., Marconi A., 2011, MNRAS, 411, 2223 (R11)
Rochais T. B., DiPompeo M. A., Myers A. D., Brotherton M. S., Runnoe J. C., Hall S. W., 2014, MNRAS, 444, 2498
Ross N. P. et al., 2012, ApJS, 199, 3
Runnoe J. C., Brotherton M. S., DiPompeo M. A., Shang Z., 2014, MNRAS, 438, 3263
Schmidt G. D., Hines D. C., 1999, ApJ, 512, 125
Schneider D. P. et al., 2010, AJ, 139, 2360
Shakura N. I., Sunyaev R. A., 1973, A&A, 24, 337
Shankar F., Dai X., Sivakoff G. R., 2008, ApJ, 687, 859
Shankar F. et al., 2016, ApJ, 818, L1
Shen Y., Ho L. C., 2014, Nature, 513, 210 (SH14)
Shen Y. et al., 2011, ApJS, 194, 45 (S11)
Shields G. A., 1978, Nature, 272, 706
Sim S. A., Proga D., Kurosawa R., Long K. S., Miller L., Turner T. J., 2012, MNRAS, 426, 2859
Smith J. E., Robinson A., Alexander D. M., Young S., Axon D. J., Corbett E. A., 2004, MNRAS, 350, 140
Stocke J. T., Morris S. L., Weymann R. J., Foltz C. B., 1992, ApJ, 396, 487
Storchi-Bergmann T., Schimoia J. S., Peterson B. M., Elvis M., Denney K. D., Eracleous M., Nemmen R. S., 2017, ApJ, 836, 236
Strateva I. V. et al., 2003, AJ, 126, 1720
Sulentic J. W., Marziani P., Dultzin-Hacyan D., 2000a, ARA&A, 38, 521
Sulentic J. W., Zwitter T., Marziani P., Dultzin-Hacyan D., 2000b, ApJ, 536, L5
Tuccillo D., Bruni G., DiPompeo M. A., Brotherton M. S., Pasetto A., Kraus A., Gonzalez-Serrano J.-I., Mack K.-H., 2017, MNRAS, preprint (arXiv:1702.01746)
Turnshek D. A., Monier E. M., Sirola C. J., Espey B. R., 1997, ApJ, 476, 40
Urry C. M., Padovani P., 1995, PASP, 107, 803
Vestergaard M., Wilkes B. J., 2001, ApJS, 134, 1
Wade R. A., 1984, MNRAS, 208, 381
Warner B., 1995, Cataclysmic Variable Stars. Cambridge Astrophysics Series, Vol. 28, Cambridge Univ. Press, Cambridge
Weymann R. J., Turnshek D. A., Christiansen W. A., 1985, in Miller J. S., ed., Astrophysics of Active Galaxies and Quasi-Stellar Objects. Univ. Science Books, Mill Valley, CA, p. 333
Weymann R. J., Morris S. L., Foltz C. B., Hewett P. C., 1991, ApJ, 373, 23
Yuan S., Strauss M. A., Zakamska N. L., 2016, MNRAS, 462, 1603
Zhang S. N., Cui W., Chen W., 1997, ApJ, 482, L155
Zhou H., Wang T., Wang H., Wang J., Yuan W., Lu Y., 2006, ApJ, 639, 716

APPENDIX A: THE ANGULAR EMISSIVITY DISTRIBUTION FROM A DISC-SHAPED LINE FORMATION REGION SUBJECT TO KEPLERIAN VELOCITY SHEAR

In the case of an optically thick line formed in a disc-shaped line formation region subject to Keplerian velocity shear, the surface brightness is (Horne & Marsh 1986)

$$J_{\rm thick}(\theta) \approx \cos\theta S_{\rm L} \Delta v \sqrt{8 \ln \tau_0}\,, \tag{A1}$$

where $S_{\rm L}$ is the line source function (assumed constant) and τ_0 is the line centre optical depth, given by

$$\tau_0 = \frac{\mathcal{W}}{\sqrt{2}\pi \Delta v \cos\theta}. \tag{A2}$$

The parameter $\mathcal{W}$ is given by

$$\mathcal{W} = \frac{\pi e^2}{m_e c} f N', \tag{A3}$$

where f is the oscillator strength and N' is the number density integrated along the vertical height of the disc-shaped emitting region. The linewidth Δv is enhanced from the thermal line width by the velocity shear, such that

$$\Delta v = \Delta v_{th} \left[1 + \left(\frac{3}{4} \frac{v_{\rm k}}{v_{\rm th}} \frac{H}{R} \right)^2 Q(\theta, \phi) \right]^{1/2}, \tag{A4}$$

where we have defined

$$Q(\theta, \phi) = \sin^2\theta \tan^2\theta \sin^2 2\phi. \tag{A5}$$

Here, ϕ is the azimuthal angle in the disc, $\nu_{\rm th}$ and $v_{\rm th}$ are the thermal line widths in frequency and velocity units, respectively, H is the scaleheight of the disc at radius R and $v_{\rm k}$ is the Keplerian velocity. The outcome of the Horne & Marsh (1986) analysis is that optically thick lines formed in a Keplerian disc are strongly anisotropic, but they do not follow a simple $\cos\theta$ distribution. Instead, the line anisotropy is a function of the velocity shear in the disc, the atomic physics of the line in question, the location of the line formation region and the vertical disc structure.

To examine the form of this line anisotropy, we can now define the angular emissivity function for a line, $\epsilon_{\rm line}(\theta)$. In the optically thick case with no additional velocity shear, $\epsilon_{0,\,\rm line}(\theta) = \cos\theta$. In the presence of Keplerian velocity shear, and neglecting the weak $\sqrt{8 \ln \tau_0}$ term, we can write

$$\epsilon_{k,\rm line}(\theta, \phi) = \cos\theta \left[1 + \left(\frac{3}{4} \frac{v_{\rm k}}{v_{\rm th}} \frac{H}{R} \right)^2 Q(\theta, \phi) \right]^{1/2}. \tag{A6}$$

This quantity is compared to $\cos\theta$ in Fig. A1 as a function of for a few values of ϕ, using typical quasar parameters of $v_{\rm k} = 10\,000\,{\rm km\,s^{-1}}$ and $v_{\rm th} = 10\,{\rm km\,s^{-1}}$, and assuming $H/R = 0.01$. We also show the azimuthally averaged function, $\bar{\epsilon}_{k,\rm line}$, which determines the integrated emergent flux as a function of θ. Fig. A2 also shows $\bar{\epsilon}_{k,\rm line}$ for a few different model values of $v_{\rm k}$, $v_{\rm th}$ and H/R; the models are defined in Table A1. Except in the case of a very thin disc ($H/R \sim 0.001$), the line emissivity does not trace $\cos\theta$ and instead is generally biased towards high inclinations. This is discussed further in Section 3.3.

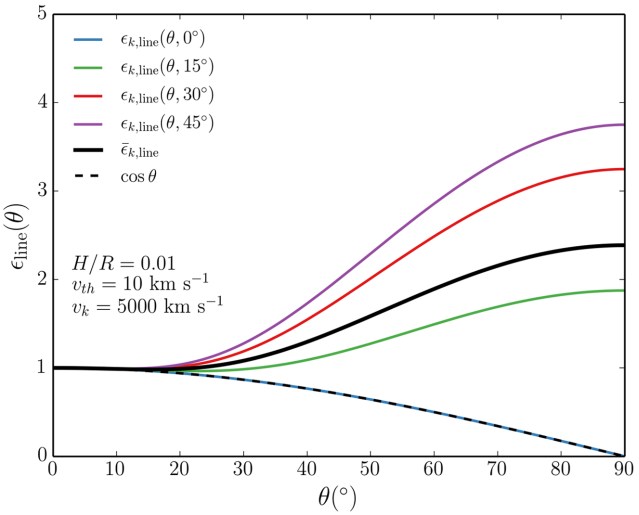

Figure A1. The line angular emissivity function, $\epsilon_{k,\mathrm{line}}(\theta, \phi)$, from a Keplerian disc as a function of inclination angle, θ, for a few different azimuthal angles, ϕ. The azimuthally averaged case, $\bar{\epsilon}_{k,\mathrm{line}}$ (thick black line), and the zero Keplerian velocity shear case, $\epsilon_{0,\mathrm{line}}(\theta) = \cos\theta$ (dotted line), are also shown.

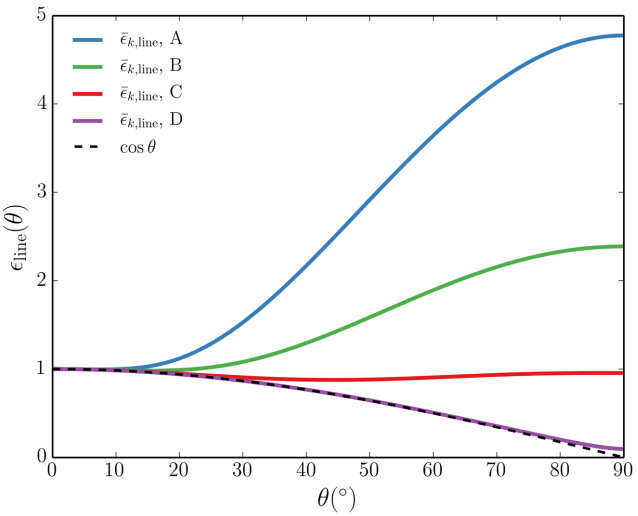

Figure A2. The azimuthally averaged line angular emissivity function, $\bar{\epsilon}_{k,\mathrm{line}}$, from a Keplerian disc as a function of inclination angle for the four models shown in Table A1. The model parameters are the values of H/R, v_{k} and v_{th}. The zero Keplerian velocity shear case, $\epsilon_{0,\mathrm{line}}(\theta) = \cos\theta$ (dotted line), is also shown. Unless the disc is very thin ($H/R \sim 0.001$), $\bar{\epsilon}_{k,\mathrm{line}}$ shows large deviations from $\cos\theta$ and is significantly more isotropic.

Table A1. The values of the Keplerian velocity, v_{k}, thermal velocity, v_{th}, and ratio of disc scaleheight to radius, H/R, for four models. These values are used as inputs to calculate $\bar{\epsilon}_{k,\mathrm{line}}$ as shown in Fig. A2, and model B is also used in Fig. A1.

Model	H/R	v_{k}(kms^{-1})	v_{th}(kms^{-1})
A	0.01	10 000	10
B	0.01	5000	10
C	0.01	5000	25
D	0.001	5000	25

This paper has been typeset from a TEX/LATEX file prepared by the author.